Carbon 191 (2022) 471–476

Contents lists available at ScienceDirect

Carbon

journal homepage: www.elsevier.com/locate/carbon

Zenith-angle resolved polarized Raman spectroscopy of graphene

Yu-Chen Leng [a, b], Tao Chen [a], Miao-Ling Lin [a], Xiao-Li Li [c], Xue-Lu Liu [a], Ping-Heng Tan [a, b, *]

[a] State Key Laboratory of Superlattices and Microstructures, Institute of Semiconductors, Chinese Academy of Sciences, Beijing, 100083, China
[b] Center of Materials Science and Optoelectronics Engineering & CAS Center of Excellence in Topological Quantum Computation, University of Chinese Academy of Sciences, Beijing, 100049, China
[c] College of Physics Science and Technology, Hebei University, Baoding, 071002, China

ARTICLE INFO

Article history:
Received 8 December 2021
Received in revised form
18 January 2022
Accepted 4 February 2022
Available online 7 February 2022

Keywords:
Zenith-angle resolved polarized Raman spectroscopy
Two dimensional materials
Interference effect

ABSTRACT

Angle resolved polarized Raman (ARPR) spectroscopy has been widely used to study basic properties of two-dimensional materials (2DMs), such as underlying symmetry, mode assignment, crystallographic orientation and optical anisotropy. The substrate effect has never been uncovered in ARPR spectroscopy. In this work, we investigated zenith-angle resolved polarized Raman (ZRPR) spectra of the G mode of graphene (1LG) deposited on different substrates as well as graphite under in-plane and out-of-plane configurations. In contrast to the independent behavior in normal incidence geometry, the G mode intensity exhibits obvious zenith-angle dependence. In particular, this polarization behavior is sensitive to the underlying substrates underneath 1LG. The ZRPR intensity of the G mode can be well understood by a model considering both Raman selection rule and zenith-angle resolved interference effect. This work enriches the understanding of polarized Raman spectroscopy of 2DMs and the approach can be applicable to other 2DMs, especially in-plane anisotropic 2DMs.

1. Introduction

Through light-matter interactions, Raman spectroscopy can provide abundant information of structural, electronic and optical properties in crystals, and has gained widespread popularity ranging from basic research to routine tests [1]. In particular, polarized Raman (PR) spectroscopy, in which the polarization of the incident photons and the scattered photons are carefully controlled in Raman experiments, the corresponding selection rules of phonon modes allow accurate characterization of crystal structures and symmetry [2,3]. In general, the PR intensity of a Raman mode is associated with its Raman tensor [4], whose form varies with the orientation of a crystal plane relative to the experimental coordinates. As a result, one can analyze and determine crystal orientation by measuring their PR intensities in different crystallographic directions [5].

For traditional three-dimensional crystals, it is easy to perform spectral analysis in a given polarization configuration [6–8]. In contrast, the PR spectra of ultrathin two-dimensional materials (2DMs) deposited on SiO_2/Si or other substrates are usually studied in normal incidence geometry, *i.e.*, the incident laser beam perpendicular to the basal plane [9]. The 2DM flake and substrate form a multilayered dielectric structure. The laser beam and Raman signal will undergo multiple reflections and refractions at the interfaces of the multilayered structure, giving rise to an interference effect [10–12]. This effect makes optical contrast of 2DM flakes dependent on the thickness of SiO_2 layer (d_{SiO2}) and the number of layers (N) of 2DM flakes, which is used to quickly identify N of 2DM flakes on SiO_2/Si substrate [13,14]. This interference effect also modulates the intensities of laser and Raman signal within the multilayered structure [10–12,15,16]. In principle, the interference effect should modulate the polarized Raman signal. However, in the normal incidence geometry, the PR spectra only reveal information related to in-plane electron momentum and electron-phonon coupling of 2DMs [17] because the polarization of electric field of incident laser is parallel to the basal plane. Therefore, all the angle resolved polarized Raman (ARPR) spectra in the normal incidence geometry are modulated to the same extent by the interference

Abbreviations: PR, polarized Raman; ARPR, Angle resolved polarized Raman; 2DMs, two-dimensional materials; ZRPR, zenith-angle resolved polarized Raman; CVD, chemical vapor deposition.

* Corresponding author. State Key Laboratory of Superlattices and Microstructures, Institute of Semiconductors, Chinese Academy of Sciences, Beijing, 100083, China.
E-mail address: phtan@semi.ac.cn (P.-H. Tan).

https://doi.org/10.1016/j.carbon.2022.02.012
0008-6223/

effect, which was not taken into account in the analysis of ARPR spectra, even for graphene-based materials [18].

Oblique incidence geometry in PR spectroscopy can introduce a zenith angle between the normal line of sample surface and the incident light. The corresponding zenith-angle resolved polarized Raman (ZRPR) spectroscopy can be an experimental method to break through the limitations in normal incidence, such as evident difference of electronic polarizability [19] and optical response [20,21] between out-of-plane and in-plane directions. Indeed, ZRPR spectroscopy had been carried out to demonstrate how the birefringence and linear dichroism effects determine ZRPR intensity of Raman modes in in-plane anisotropic layered materials, such as bulk black phosphorus [22]. How the interference effect affects ZRPR spectra of ultrathin 2DM flakes deposited on multilayered dielectric substrates is a basic issue for PR spectroscopy of 2DMs.

Here, by taking monolayer graphene (1LG) as an example, we investigated ZRPR spectroscopy of 1LG at oblique laser incidence. The Raman intensity ratio of the G mode between out-of-plane and in-plane configurations, $I_{out}(G)/I_{in}(G)$, exhibits obvious dependence on zenith-angle and substrate. A quantitative model based on interference effect was proposed to understand the ZRPR intensity of the G mode, which shows that the G mode intensity is sensitive to d_{SiO2} of the substrate. This work demonstrates that multilayered dielectric substrates can significantly modify ZRPR intensity of few-layer 2DMs, which had never explored in the present ARPR spectroscopy.

2. Experimental

2.1. Synthesis and transfer of 1LG

Monolayer graphene (1LG) was grown on 25-μm thick Cu foils (Alfa Aesar, 99.8%) by a plasma-enhanced chemical vapor deposition (CVD) system [23]. The Cu substrate was heated to 830 °C at a heating rate of 3 °Cs^{-1}. Then H_2 gas was introduced into the chamber at a flow rate of 40 standard cubic centimeters per minute (sccm) and discharged for 2 min at a radio-frequency power of 50 W to eliminate surface oxides on the copper foil. After that, the chamber was purged with Ar at a flow rate of 100 sccm for 2 min to remove residual hydrogen gas. Under a continuous flow of argon (40 sccm) and methane (1 sccm), 1LG was synthesized in 3 min at a plasma power of 50W, while the pressure was kept at 10 mTorr.

After cooling down the samples to room temperature, the synthesized 1LG were transferred onto three different substrates (95nm-SiO_2/Si, 297nm-SiO_2/Si and quartz) [20]. The polymethyl methacrylate (PMMA) solution was spin-coated on 1LG/Cu and baked at 150 °C for 3 min to generate the PMMA film. Then the Cu foil was dissolved in aqueous solution of $FeCl_3$. After that, the PMMA/1LG membrane was cleaned with deionized water and placed on 95nm-SiO_2/Si, 297nm-SiO_2/Si and quartz substrates to form the PMMA/1LG/substrate structure. The thickness of SiO_2 film had been determined by the optical contrast method [24]. Finally, the PMMA film was removed by acetone.

2.2. Raman measurements

The zenith-angle resolved polarized Raman (ZRPR) spectra were measured at room temperature by using a Jobin-Yvon HR-Evolution micro-Raman system equipped with a liquid-nitrogen-cooled charge-coupled device detector (CCD). The excitation wavelength is 532 nm from a solid state laser. The 600 lines/mm grating was used in the Raman measurements, which enables each CCD pixel to cover 0.85 cm^{-1} at 532 nm. The laser power density was kept below 0.5 mW/μm^2 to avoid heating the samples. The acquisition time is 200 s to ensure the high signal-to-noise ratio of the Raman spectra.

Fig. 1 demonstrates schematic diagram of the polarization configurations in the ZRPR measurements. The sample on the substrate is placed vertically. In the laboratory coordinate XYZ as denoted in lower left quarter of Fig. 1, the laser polarization vector after the polarizer is along Y. Then, the laser beam propagates through a half-wave plate with its initial fast axis along Y, and is further focused onto the sample basal plane by a lens (NA = 0.08), leading to a circular-laser spot with a diameter of 10 μm at normal incidence and angle resolution of 8.7° for ZRPR measurements. The Raman signal collected by the same lens propagates back through the same half-wave plate. Then, it is selected by an analyzer with polarization parallel to that of the polarizer. At last, it is focused into a spectrometer for Raman measurements. By varying the fast axis of the half-wave plate, the laser polarization vector at the sample basal plane can be fixed along Y or X, while the collected Raman signal is always along Y.

When the laser is initially focused in normal incidence onto the graphene plane, we can denote crystal coordinates (xyz) according to XYZ. By switching the fast axis of the half-wave plate between 0° and 45°, the polarization vectors of the incident laser and the scattered Raman signal are always parallel to the graphene plane. However, when the sample is rotated by an angle of θ_0, as shown in the inset to Fig. 1, the angle between the laser excitation and the normal of graphene plane is θ_0, *i.e.*, the zenith angle of the laser excitation in the crystal coordinates of sample. When the fast axis of half-wave plate is along Y, the laser polarization vector at the sample is fully contained in the graphene basal plane (so-called in-plane configuration, the vector along Y). When the fast axis is rotated by 45° relative to Y, the laser polarization vector is along X, exhibiting an angle of θ_0 away from the graphene plane (so-called out-of-plane configuration). One can measure ZRPR spectra in the in-plane and out-of-plane configurations, and the corresponding Raman mode intensities are denoted as I_{in} and I_{out}, respectively.

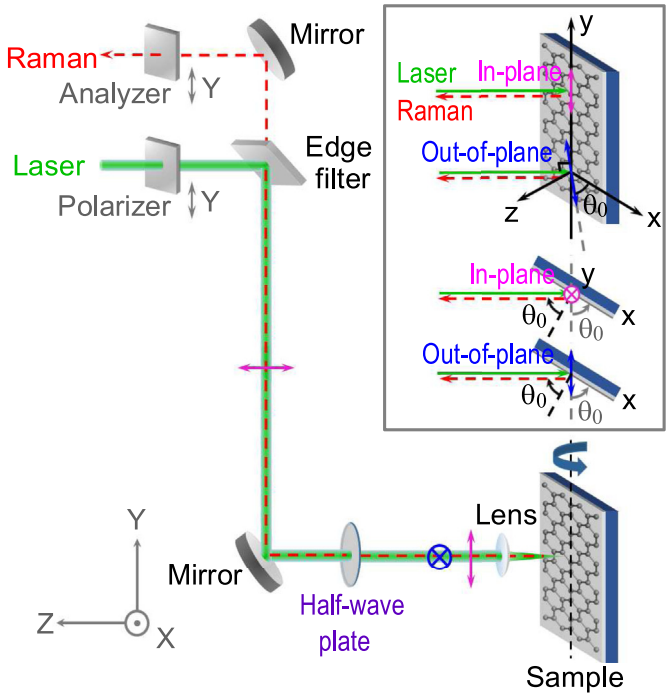

Fig. 1. Schematic diagram of the experimental setup. The polarization of laser and Raman signal is altered by a half-wave plate, and the zenith-angle θ_0 is changed by rotating the sample. The inset shows schematic diagrams of in-plane and out-of-plane configurations in a side view and top view. (A colour version of this figure can be viewed online.)

3. Results and discussions

Raman spectra of graphene samples collected at normal laser incidence, as well as their optical images are depicted in Fig. 2, in which the G (~1582 cm^{-1}) and 2D (~2684 cm^{-1}) modes are shown. Highly oriented pyrolytic graphite was used as a reference in the measurements and its Raman spectra are also shown. The symmetric single Lorentzian lineshape of the 2D mode in graphene samples indicates that each graphene sample is mainly 1LG [25,26]. The weak D mode suggests high crystal quality of 1LG. The asymmetric peak at ~1554 cm^{-1} in all the samples originates from the vibration of oxygen molecules in air [27]. In this work, the G mode with E_{2g} symmetry is chosen to investigate the ZRPR intensity of each graphene sample.

The typical ZRPR spectra of 1LG on different substrates are depicted in Fig. 3a–c. When $\theta_0 = 0°$, the G mode intensities of each sample in out-of-plane and in-plane configurations, *i.e.*, $I_{out}(G)$ and $I_{in}(G)$, are identical to each other due to the in-plane isotropy of the G mode. As θ_0 increases, $I_{out}(G)$ gradually deviates from $I_{in}(G)$. Note that the G mode of 1LG/297nm-SiO_2/Si blue shifts up to ~ 1594 cm^{-1}, resulting from the doping induced by charge transfer in the CVD growth and transfer process [28]. Because the G mode of the three samples exhibits an asymmetric line shape, we use the integral intensity of the G mode to analyze its ZRPR intensity.

The ZRPR intensity ratio of the G mode for the three 1LG samples in out-of-plane and in-plane configurations, $I_{out}(G)/I_{in}(G)$, are summarized in Fig. 3d and e. $I_{out}(G)/I_{in}(G)$ show significant dependence on the substrates. For 1LG/95nm-SiO_2/Si, $I_{out}(G)/I_{in}(G)$ (open diamonds) decreases monotonically to 0.2 with increasing θ_0 up to 60°. While for 1LG/297nm-SiO_2/Si, $I_{out}(G)/I_{in}(G)$ first decreases as θ_0 increases, reaching a minimum (0.6) at $\theta_0 = 40°$, and then monotonically increases to 1.5 at $\theta_0 = 60°$. As for 1LG/quartz, $I_{out}(G)/I_{in}(G)$ (open squares) monotonically decreases to 0.6 with a relatively flat trend as θ_0 increases up to 60°.

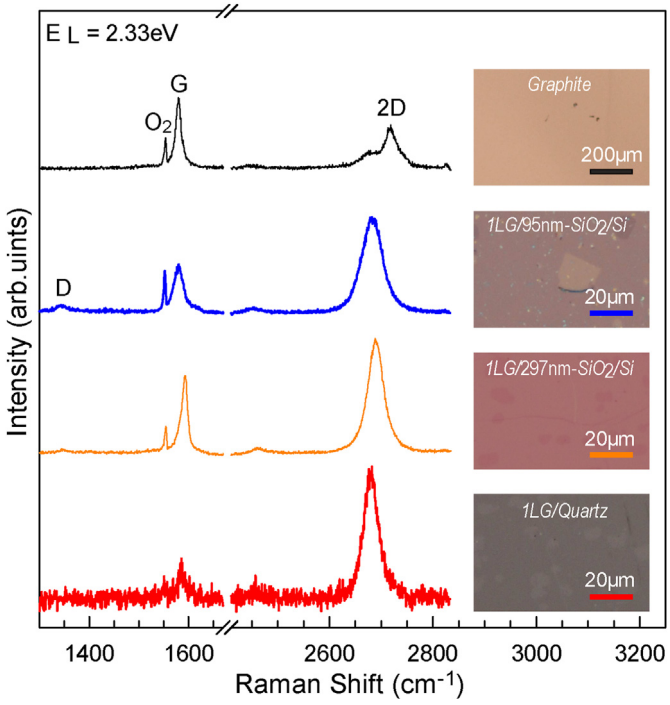

Fig. 2. Raman spectra of 1LG/95nm-SiO_2/Si, 1LG/297nm-SiO_2/Si, 1LG/quartz, and bulk graphite at normal incidence. Their corresponding optical images are shown on the right. (A colour version of this figure can be viewed online.)

To understand the substrate-dependent ZRPR intensity, not only the Raman selection rule but also the θ_0-dependent interference effect should be considered. For a general case of Raman scattering, the intensity of a Raman mode is associated with its Raman tensors based on the Raman selection rule as $I \propto \sum_j \left| \mathbf{e}_r \cdot \mathbf{R}^j \cdot \mathbf{e}_l \right|^2$, where $\mathbf{R}^j$ is the j^{th} Raman tensor of the Raman mode, $\boldsymbol{e}_r$ and $\boldsymbol{e}_l$ represent the polarization vectors of the Raman signal and laser excitation, respectively. $\mathbf{R}^j$ with elements $R^j_{uv}(u, v = x, y, z)$ has a certain form related to the symmetry of the crystals [4]. In graphene, the two Raman tensors of the G mode are as follows,

$$\mathbf{R}^1(G) = \begin{pmatrix} a & 0 & 0 \\ 0 & -a & 0 \\ 0 & 0 & 0 \end{pmatrix}, \mathbf{R}^2(G) = \begin{pmatrix} 0 & a & 0 \\ a & 0 & 0 \\ 0 & 0 & 0 \end{pmatrix}. \quad (1)$$

For ZRPR spectroscopy, due to the high optical transmittance of 1LG and SiO_2, multiple reflections at the interfaces and optical interference within the multilayered structure of air/1LG/SiO_2/Si or air/1LG/quartz will significantly affect the electric fields of both laser excitation and Raman signal. The optical path of the laser beam in 1LG/SiO_2/Si and 1LG/quartz with zenith angle of θ_0 are indicated in Fig. 4a and b, respectively. Since the NA of the lens used in the experiment is small, here we ignore the uncertainty of θ_0 caused by lens focusing. The electric field vector of the incident laser can be classified into *s*-($E^s_{01,l}$) and *p*-polarization ($E^p_{01,l}$), in which the *s*(*p*)-polarization is perpendicular (parallel) to the incident plane. The electric field of incident laser inside 1LG, with a propagation distance of z_1, are denoted as $E^{s(p)}_{1,l}(z_1) = F^{s(p)}_l(z_1)E^{s(p)}_{01,l}$, where $F^{s(p)}_l(z_1)$ stands for the electric field enhancement factor at z_1 caused by the interference effect [10–12] (See Supplementary data for more details), $E^{s(p)}_{01,l}$ is the electric field of the incident laser excitation in air.

In the out-of-plane configuration, the electric field $E^p_{1,l}(z_1)$ can be decomposed into two components along its *x* and *z* axes, *i.e.*,

$$\begin{aligned} E^x_{1,l}(z_1) &= E^p_{01,l} \cdot e^x_l \cdot F^x_l(z_1), \\ E^z_{1,l}(z_1) &= E^p_{01,l} \cdot e^z_l \cdot F^z_l(z_1), \end{aligned} \quad (2)$$

where $e^x_l = cos\theta_1$ and $e^z_l = sin\theta_1$ are the laser polarization vectors along the *x* and *z* axes, respectively, θ_1 is the refraction angle corresponding to θ_0. The electric field of Raman signal at z_1, $E^u_{1,r}(z_1)(u = x, y, z)$ can be given by $E^v_{1,l}(z_1)$ and the Raman tensor, *i.e.*,

$$E^{u,j}_{1,r}(z_1) = \sum_{v=x,y,z} R^j_{uv} E^v_{1,l}(z_1). \quad (3)$$

Similar to the incident process, Raman signals are also affected by the interference effect, and the corresponding electric field enhancement factor at z_1 is denoted as $F^u_r(z_1)$ (See Supplementary data for more details). The electric field components of the collected Raman signal in air are given by

$$\begin{aligned} E^{x,j}_{01,r} &= F^x_r(z_1) \cdot e^x_r \cdot E^{x,j}_{1,r}(z_1), \\ E^{z,j}_{01,r} &= F^z_r(z_1) \cdot e^z_r \cdot E^{z,j}_{1,r}(z_1) \end{aligned} \quad (4)$$

where $e^x_r = cos\theta_1$ and $e^z_r = sin\theta_1$ are the polarization vectors of Raman signal along the *x* and *z* axes, respectively. Therefore, the Raman intensity is obtained by summing the squares of electric field components integrating over the thickness (d_1) of graphene layers as follows,

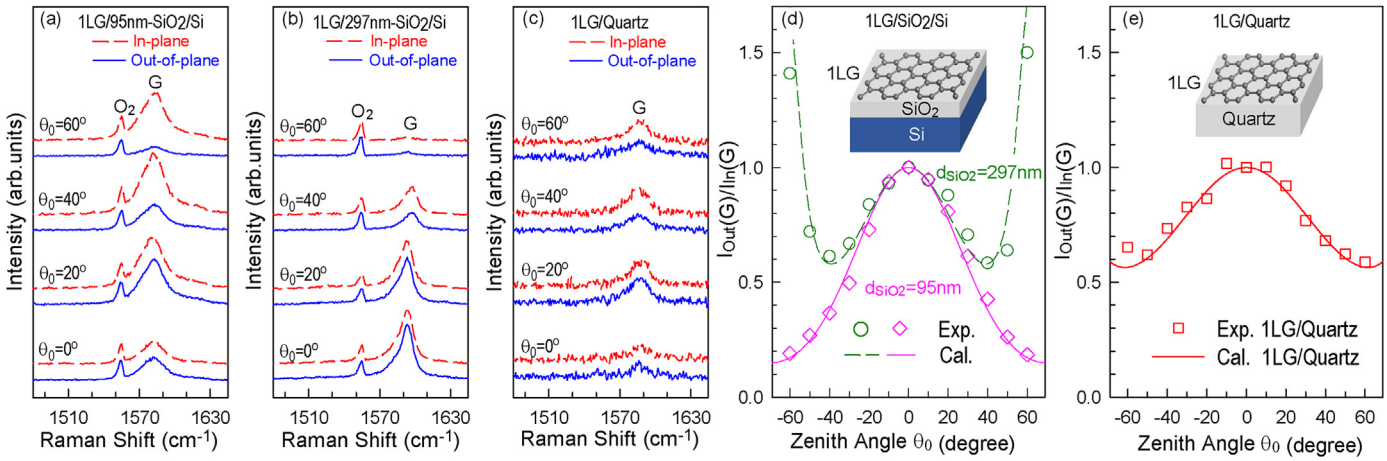

Fig. 3. Typical ZRPR spectra of 1LG on (a) 95 nm-SiO_2/Si, (b) 297 nm-SiO_2/Si and (c) quartz under in-plane and out-of-plane configurations excited at 532 nm. The experimental (open circles, diamonds and squares) and calculated (dashed and solid lines) θ_0-dependent $I_{out}(G)/I_{in}(G)$ of 1LG on (d) 95nm-SiO_2/Si, 297nm-SiO_2/Si and (e) quartz are also shown. (A colour version of this figure can be viewed online.)

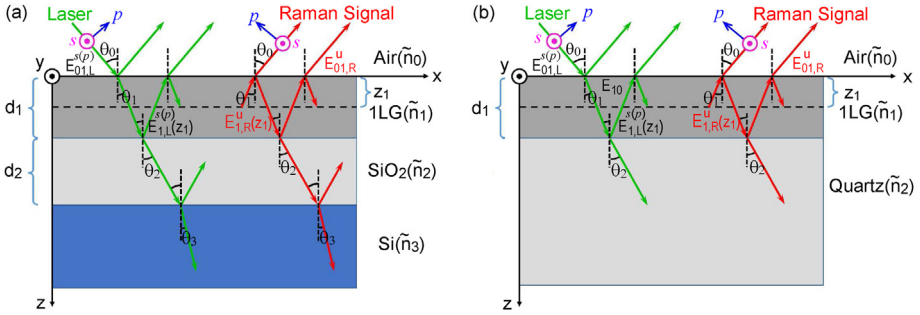

Fig. 4. Schematics of propagation path of laser (green) and scattered Raman signal (red) for (a) 1LG/SiO_2/Si and (b) 1LG/quartz. (A colour version of this figure can be viewed online.)

$$I \propto \sum_{j=1,2} \sum_{u=x,y,z} \left| \int_0^{d_1} E_{01,r}^{u,j} dz_1 \right|^2 \tag{5}$$

$$= E_{01,l}^{p} \sum_{j=1,2} \sum_{u=x,y,z} \left| \int_0^{d_1} F_r^u(z_1) \cdot e_r^u \cdot \sum_{v=x,y,z} R_{uv}^j \cdot e_l^v \cdot F_l^v(z_1) dz_1 \right|^2 \tag{6}$$

The in-plane configuration case is simpler, because only the electric field component along the y axis exists. The corresponding electric fields of the incident laser and Raman signal are, respectively,

$$\begin{aligned} E_{1,l}^{y}(z_1) &= E_{01,l}^{s} F_l^y(z_1), \\ E_{01,r}^{y,j} &= F_r^y(z_1) E_{1,r}^{y,j}(z_1). \end{aligned} \tag{7}$$

Then the ZRPR intensity of the G mode in the in-plane configuration can be calculated by Eq. (5). The calculated θ_0-dependent $I_{out}(G)/I_{in}(G)$ of the three 1LG samples are included in Fig. 3d and e, which are in line with the experimental results. In principle, the model described by Eq. (5) can be applicable to 2D mode whose polarization behavior can be expressed by an effective Raman tensor with A_{1g} symmetry [29,30]. The θ_0-dependent $I_{out}(2D)/I_{in}(2D)$ of the three 1LG samples are included in Fig. S3. The good agreement between experimental and theoretical results again proves the reliability of the proposed model.

The ZRPR spectra for graphite were also measured and depicted in Fig. 5a. With increasing θ_0, $I_{out}(G)/I_{in}(G)$ increases monotonically. Intuitively, the p-wave (out-of-plane configuration) exhibits an electric field oriented at an angle respect to the graphene plane, it seems that only the in-plane electric field component contributes to $I_{out}(G)$. Based on $I \propto \sum_j \left| \mathbf{e}_r \cdot \mathbf{R}^j \cdot \mathbf{e}_l \right|^2$, one expects that $I_{out}(G)$ is proportional to $cos^4(\theta_0)$ as determined by Raman tensors of the G mode. Therefore, $I_{out}(G)$ should be relatively weaker than $I_{in}(G)$, which is inconsistent with the experimental data. Indeed, the experimental $I_{out}(G)/I_{in}(G)$ summarized in Fig. 5b approaches up to almost 5 at $\theta_0 = 70°$. To understand the increase in $I_{out}(G)/I_{in}(G)$ with increasing θ_0, it is necessary to consider not only the Raman selection rule but also the reflections of laser excitation and Raman signal at air/graphite interface. The θ_0-dependent reflectivity of s-(R_s) and p-polarization (R_p) components of laser excitation can be obtained by the relative intensity of reflected laser to the incident laser at the air/graphite interface under in-plane and out-of-plane configurations, respectively. The calculated θ_0-dependent R_s and R_p of graphite by Fresnel's law are depicted in the inset to Fig. 5b, which are in perfect agreement with the experimental one. As θ_0 increases from 0° to 70°, R_p decreases while R_s increases monotonically. Therefore, the power of laser excitation penetrating through the air/graphite interface under the out-of-plane configuration is larger than that under the in-plane configuration, which is also true for the Raman signal. This leads to larger $I_{out}(G)$ than $I_{in}(G)$. To simplify the case of $I_{out}(G)/I_{in}(G)$ for graphite, we use an average refractive index $\tilde{n}_1$ of 2.50 + 1.40i for s- and p-polarization components of both laser excitation at 532 nm and Raman signal at 581 nm, then, $I_{out}(G)/I_{in}(G)$ of graphite can be reduced to

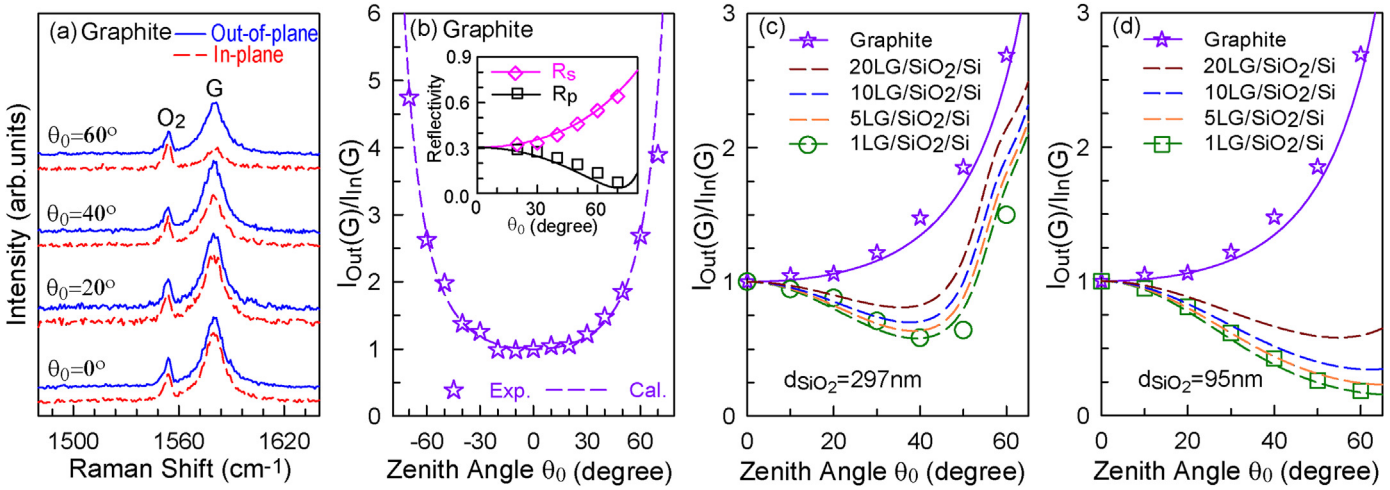

Fig. 5. (a) Typical ZRPR spectra of graphite excited at 532 nm under in-plane and out-of-plane configurations. (b) The experimental (open stars) θ_0-dependent $I_{out}(G)/I_{in}(G)$ of graphite and the calculated (dashed line) one by eq (8). The inset to (b) shows the experimental reflectivity (open diamonds and squares) and calculated curves (solid lines) of *s*-(R_s) and *p*-polarization (R_p) laser under in-plane and out-of-plane configurations. The calculated θ_0-dependent $I_{out}(G)/I_{in}(G)$ of *N*LG on (c) 297nm-SiO_2/Si and (d) 95nm-SiO_2/Si along with that of graphite by eq (5), and the corresponding experimental data of 1LG and graphite are also included. (A colour version of this figure can be viewed online.)

$$I_{out}(G)\Big/I_{in}(G)\propto\frac{t_{01}^{p}\cdot t_{10}^{p}{}^{2}}{t_{01}^{s}\cdot t_{10}^{s}{}^{2}}cos^{4}\theta_1=\frac{t_{01}^{p}\cdot t_{10}^{p}{}^{2}}{t_{01}^{s}\cdot t_{10}^{s}{}^{2}}\left(1-\frac{sin^{2}\theta_0}{\overline{n}_1^{2}}\right)^{2},\quad(8)$$

in which $t_{01}^{s(p)}$ and $t_{10}^{s(p)}$ are the transmission coefficients of *s*(*p*)-polarization components of laser excitation at air/graphite and graphite/air interfaces, respectively (See Supplementary data for more details). The calculated $I_{out}(G)/I_{in}(G)$ by Eq. (8) is depicted by dash line in Fig. 5b, which can well describe the tendency of $I_{out}(G)/I_{in}(G)$ with θ_0.

In principle, the model described by Eq. (5) can be applicable to graphite and multilayer graphene deposited on SiO_2/Si substrate, the former can be considered as multilayer graphene with infinite number of layers. Here we calculated $I_{out}(G)/I_{in}(G)$ of *N*-layer graphene (*N*LG, $N = 1, 5, 10$ and 20) on 297nm-SiO_2/Si and 95nm-SiO_2/Si substrate by Eq. (5), as shown in Fig. 5c and d, respectively. With increasing *N*, the θ_0-dependent $I_{out}(G)/I_{in}(G)$ curves rise gradually due to the modulation of the interference effect by *N*LG, and finally approach to the graphite case.

4. Conclusion

In summary, ZRPR spectra of 1LG on several substrates were measured under in-plane and out-of-plane configurations, which exhibit obvious dependence on zenith-angle and substrate. The corresponding θ_0-dependent $I_{out}(G)/I_{in}(G)$ of 1LG can be well understood and reproduced by a quantitative model with the interference effect considered. This model can also explain the experimental θ_0-dependent $I_{out}(G)/I_{in}(G)$ of graphite, where $I_{out}(G)$ is also stronger than $I_{in}(G)$ because more *p*-polarization component of laser excitation penetrated into graphite to excite the corresponding Raman signal. The ZRPR spectroscopy can break through the limitations in normal incidence Raman spectroscopy and detect the properties of out-of-plane symmetry in graphene. This work demonstrates the importance of the interference effect in understanding ZRPR spectroscopy of graphene flakes deposited on multilayer dielectric substrate and provides a theoretical basis for quantitative analysis of ZRPR spectra, which is of great significance for the characterization of 2DMs and the application of related devices.

CRediT authorship contribution statement

Yu-Chen Leng: Data curation, Investigation, Software, Formal analysis, Writing – original draft. **Tao Chen:** Investigation, Methodology, Validation, Writing – original draft. **Miao-Ling Lin:** Writing – original draft. **Xiao-Li Li:** Software. **Xue-Lu Liu:** Methodology. **Ping-Heng Tan:** Conceptualization, Writing – review & editing, Supervision, Project administration, Funding acquisition.

Declaration of competing interest

The authors declare that they have no known competing financial interests or personal relationships that could have appeared to influence the work reported in this paper.

Acknowledgments

We acknowledge support from National Natural Science Foundation of China (Grant Nos. 12004377 and 11874350) and CAS Key Research Program of Frontier Sciences (Grant Nos. ZDBS-LY-SLH004 and XDPB22).

Appendix A. Supplementary data

Supplementary data to this article can be found online at https://doi.org/10.1016/j.carbon.2022.02.012.

References

[1] P.H. Tan, Raman Spectroscopy of Two-Dimensional Materials, Springer Nature Singapore Pte Ltd., Singapore, 2019, https://doi.org/10.1007/978-981-13-1828-3.
[2] J. Kim, J.U. Lee, H. Cheong, Polarized Raman spectroscopy for studying two-dimensional materials, J. Phys. Condens. Matter 32 (34) (2020) 343001, https://doi.org/10.1088/1361-648x/ab8848.
[3] B. Xu, N. Mao, Y. Zhao, L. Tong, J. Zhang, Polarized Raman spectroscopy for determining crystallographic orientation of low-dimensional materials, J. Phys. Chem. Lett. 12 (31) (2021) 7442–7452, https://doi.org/10.1021/acs.jpclett.1c01889.
[4] R. Loudon, The Raman effect in crystals, Adv. Phys. 13 (52) (1964) 423–482, https://doi.org/10.1080/00018730110101395.
[5] X.L. Liu, X. Zhang, M.L. Lin, P.H. Tan, Different angle-resolved polarization configurations of Raman spectroscopy: a case on the basal and edge plane of two-dimensional materials, Chin. Phys. B 26 (6) (2017), 067802, https://doi.org/10.1088/1674-1056/26/6/067802.

[6] J. Mossbrucker, T.A. Grotjohn, Determination of local crystal orientation of diamond using polarized Raman spectra, Diam. Relat. Mater. 5 (11) (1996) 1333–1343, https://doi.org/10.1016/0925-9635(96)00547-X.
[7] J. Thyr, L. Österlund, T. Edvinsson, Polarized and non-polarized Raman spectroscopy of ZnO crystals: method for determination of crystal growth and crystal plane orientation for nanomaterials, J. Raman Spectrosc. 52 (8) (2021) 1395–1405, https://doi.org/10.1002/jrs.6148.
[8] W. Qiu, L.L. Ma, H.D. Xing, C.L. Cheng, G.Y. Huang, Spectral characteristics of (111) silicon with Raman selections under different states of stress, AIP Adv. 7 (7) (2017), 075002, https://doi.org/10.1063/1.4992106.
[9] X. Zhang, X.F. Qiao, W. Shi, J.B. Wu, D.S. Jiang, P.H. Tan, Phonon and Raman scattering of two-dimensional transition metal dichalcogenides from monolayer, multilayer to bulk material, Chem. Soc. Rev. 44 (2015) 2757–2785, https://doi.org/10.1039/c4cs00282b.
[10] Y.Y. Wang, Z.H. Ni, Z.X. Shen, H.M. Wang, Y.H. Wu, Interference enhancement of Raman signal of graphene, Appl. Phys. Lett. 92 (4) (2008), 043121, https://doi.org/10.1063/1.2838745.
[11] D. Yoon, H. Moon, Y.W. Son, J.S. Choi, B.H. Park, Y.H. Cha, et al., Interference effect on Raman spectrum of graphene on SiO_2/Si, Phys. Rev. B 80 (12) (2009) 125422, https://doi.org/10.1103/PhysRevB.80.125422.
[12] X.L. Li, X.F. Qiao, W.P. Han, Y. Lu, Q.H. Tan, X.L. Liu, et al., Layer number identification of intrinsic and defective multilayered graphenes up to 100 layers by the Raman mode intensity from substrates, Nanoscale 7 (17) (2015) 8135–8141, https://doi.org/10.1039/C5NR01514F.
[13] Z.H. Ni, H.M. Wang, J. Kasim, H.M. Fan, T. Yu, Y.H. Wu, et al., Graphene thickness determination using reflection and contrast spectroscopy, Nano Lett. 7 (9) (2007) 2758–2763, https://doi.org/10.1021/nl071254m.
[14] W.P. Han, Y.M. Shi, X.L. Li, S.Q. Luo, Y. Lu, P.H. Tan, The numerical-aperture-dependent optical contrast and thickness determination of ultrathin flakes of two-dimensional atomic crystals: a case of graphene multilayers, Acta Phys. Sin. 62 (11) (2013) 110702, https://doi.org/10.7498/aps.62.110702.
[15] Y.K. Koh, M.H. Bae, D.G. Cahill, E. Pop, Reliably counting atomic planes of few-layer graphene (n>4), ACS Nano 5 (1) (2011) 269–274, https://doi.org/10.1021/nn102658a.
[16] X.L. Li, X.F. Qiao, W.P. Han, X. Zhang, Q.H. Tan, T. Chen, et al., Determining layer number of two-dimensional flakes of transition-metal dichalcogenides by the Raman intensity from substrates, Nanotechnology 27 (14) (2016) 145704, https://doi.org/10.1088/0957-4484/27/14/145704.
[17] D. Yoon, H. Moon, Y.W. Son, G. Samsonidze, B.H. Park, J.B. Kim, et al., Strong polarization dependence of double-resonant Raman intensities in graphene, Nano Lett. 8 (12) (2008) 4270–4274, https://doi.org/10.1021/nl8017498.
[18] J.B. Wu, M.L. Lin, X. Cong, H.N. Liu, P.H. Tan, Raman spectroscopy of graphene-based materials and its applications in related devices, Chem. Soc. Rev. 47 (5) (2018) 1822–1873, https://doi.org/10.1039/c6cs00915h.
[19] T. Tian, D. Scullion, D. Hughes, L.H. Li, C.J. Shih, J. Coleman, et al., Electronic polarizability as the fundamental variable in the dielectric properties of two-dimensional materials, Nano Lett. 20 (2) (2020) 841–851, https://doi.org/10.1021/acs.nanolett.9b02982.
[20] G. Heo, Y.S. Kim, S.H. Chun, M.J. Seong, Polarized Raman spectroscopy with differing angles of laser incidence on single-layer graphene, Nanoscale Res. Lett. 10 (1) (2015) 45, https://doi.org/10.1186/s11671-015-0743-4.
[21] L. Matthes, O. Pulci, F. Bechstedt, Influence of out-of-plane response on optical properties of two-dimensional materials: first principles approach, Phys. Rev. B 94 (2016) 205408, https://doi.org/10.1103/PhysRevB.94.205408.
[22] M.L. Lin, Y.C. Leng, X. Cong, D. Meng, J. Wang, X.L. Li, et al., Understanding angle-resolved polarized Raman scattering from black phosphorus at normal and oblique laser incidences, Sci. Bull. 65 (22) (2020) 1894–1900, https://doi.org/10.1016/j.scib.2020.08.008.
[23] Y.S. Kim, J.H. Lee, Y.D. Kim, S.K. Jerng, K. Joo, E. Kim, et al., Methane as an effective hydrogen source for single-layer graphene synthesis on cu foil by plasma enhanced chemical vapor deposition, Nanoscale 5 (2013) 1221–1226, https://doi.org/10.1039/C2NR33034B.
[24] Y. Lu, X.L. Li, X. Zhang, J.B. Wu, P.H. Tan, Optical contrast determination of the thickness of SiO_2 film on Si substrate partially covered by two-dimensional crystal flakes, Sci. Bull. 60 (8) (2015) 806–811, https://doi.org/10.1007/s11434-015-0774-3.
[25] A.C. Ferrari, J.C. Meyer, V. Scardaci, C. Casiraghi, M. Lazzeri, F. Mauri, et al., Raman spectrum of graphene and graphene layers, Phys. Rev. Lett. 97 (2006) 187401, https://doi.org/10.1103/PhysRevLett.97.187401.
[26] W.J. Zhao, P.H. Tan, J. Zhang, J. Liu, Charge transfer and optical phonon mixing in few-layer graphene chemically doped with sulfuric acid, Phys. Rev. B 82 (2010) 245423, https://doi.org/10.1103/PhysRevB.82.245423.
[27] Y. Numata, Y. Shinohara, T. Kitayama, H. Tanaka, Rapid and accurate quantitative analysis of fermentation gases by Raman spectroscopy, Process Biochem. 48 (4) (2013) 569–574, https://doi.org/10.1016/j.procbio.2013.02.018.
[28] W.J. Zhao, P.H. Tan, J. Liu, A.C. Ferrari, Intercalation of few-layer graphite flakes with $FeCl_3$: Raman determination of fermi level, layer by layer decoupling, and stability, J. Am. Chem. Soc. 133 (2011) 5941–5946, https://doi.org/10.1021/ja110939a.
[29] Z. Li, R.J. Young, I.A. Kinloch, N.R. Wilson, A.J. Marsden, A.P.A. Raju, Quantitative determination of the spatial orientation of graphene by polarized Raman spectroscopy, Carbon 88 (2015) 215–224, https://doi.org/10.1016/j.carbon.2015.02.072.
[30] J.E. Proctor, E. Gregoryanz, K.S. Novoselov, M. Lotya, J.N. Coleman, M.P. Halsall, High-pressure Raman spectroscopy of graphene, Phys. Rev. B 80 (2009), 073408, https://doi.org/10.1103/PhysRevB.80.073408.